

COVER PAGE

Document downloaded by @DAEL

Sun Nov 29 10:06:07 2026
For personal use

When automatic English translation is provided, only the original document is authentic.
The EAA cannot be held responsible of any translation error

Bibliographical reference

Coupled Finite Element: Series Expansion Method for the Modeling of Directional Piezoelectric Sources Radiating in an Elastic Formation, Madjid Berraki, Bertrand Dubus and Axelle Baroni, Acta Acustica **vol. 94** (Number 5), 2008, pp. 656-667

DOI
https://doi.org/10.3813/AAA.918080

ACTA ACUSTICA UNITED WITH ACUSTICA
Vol. 94 (2008) 656 – 667

DOI 10.3813/AAA.918080

Coupled Finite Element: Series Expansion Method for the Modeling of Directional Piezoelectric Sources Radiating in an Elastic Formation

Madjid Berraki[1,2),*], Bertrand Dubus[1)], Axelle Baroni[2)]

[1)] Institut d'Électronique de Microélectronique et de Nanotechnologie, Département ISEN, UMR CNRS 8520, 41 boulevard Vauban, 59046 Lille cedex, France

[2)] Institut Français du Pétrole, Division Géophysique, 1&4 Avenue de Bois-Préau, 92852 Rueil Malmaison cedex, France

Summary

A numerical method is proposed to describe, in the frequency domain, the elastic waves radiated from a piezoelectric transducer in an infinite elastic formation in the rotational symmetric case. It relies upon the coupling between the Finite Element Method, to model the transducer and the surrounding formation up to a spherical boundary, and a series expansion, to model the field on and outside the boundary. Validation tests conducted on point force show that the accuracy of the results is mainly determined by the number of terms used in the series expansion which has to be increased when the frequency increases. The method is applied to the design of a directional piezoelectric source. The directional radiation is obtained by controlling electrically the symmetrical and anti-symmetrical vibrations of a double-ended longitudinal vibrator. The control law on electrical excitation is extracted from the numerical computation and a directional radiation is obtained for both longitudinal and transverse waves.

PACS no. 43.20.Rz, 43.38.Fx

1. Introduction

The seismic method, used for imaging the subsurface, relies upon the propagation time analysis of elastic waves between a source and a receiver, either located at the surface or buried. In time-lapse or 4D seismics [1, 2, 3, 4], the aim is to monitor the changes in the subsurface with time by repeating seismic measurements with the same three dimensional configuration. Reliability and repeatability of the acquisition footprint are therefore considered as key requirements. Piezoelectric transducers, which are not emitting enough energy for conventional seismics, have drawn interest for 4D seismics because of their high repeatability [5]. With classical surface or buried seismic sources, the weathered zone, a 10 to 20 m thick layer located below the earth surface, whose physical properties vary with the weathering, is an additional source of signal fluctuation. With a view to eliminate this perturbation, the concept of a piezoelectric directional source, buried below the weathered zone and radiating downwards has recently been investigated [6, 7].

In the frequency domain, piezoelectric directional sources can be obtained by combining modes of vibration excited with adequate amplitudes and phases. Such a concept has been developed for sonar sources by combining monopole and dipole radiations and has led to the realization of flextensional projectors with directional radiation patterns [8, 9, 10]. Sonar and seismic sources exhibit different directivity patterns. In underwater acoustics, only one spherical pressure wave can propagate in the far-field and radiation patterns are mainly monopolar or dipolar at low frequency. The directional radiation is obtained by prescribing one additional condition (cancellation of the far-field radiation in the θ-direction for example) which determines the relative amplitudes and phases of monopolar and dipolar radiation modes. In seismics, three (one longitudinal and two transverse) spherical waves can propagate in the far-field. Monopolar sources cannot be realized (except with explosives) and ideal sources have either dipolar (point force) or more complicated (couple of forces with or without moment) directivity patterns. By combining two ideal sources, only one additional condition is prescribed and therefore, the directionality is enforced for only one wave in the far-field. Another difference between sonar and seismics is the small size of the

Received 15 January 2008, revised 25 June 2008, accepted 18 August 2008.

* Now at SERCEL SA, Marine Sources Division, Z.I. Toulon Est, 105 rue Pasteur, 83210 La Farlede, France

© S. Hirzel Verlag · EAA

source with respect to the wavelength which prevents the use of transducer resonances. Despite these restrictions, the combination of two point forces (or one point force and one couple of forces without moment) excited with adequate amplitudes and phases has been found to be reasonably directional for both the longitudinal and transverse waves [6, 7]. In the present work, the possibility to design a directional piezoelectric source based on this combination for seismics is investigated.

To describe piezoelectric transducers radiating in an infinite medium, numerical models in the frequency domain are usually based on the finite element modeling of an internal finite domain that includes the transducer up to an artificial boundary on which appropriate conditions are prescribed. Two classes of boundary conditions are usually distinguished: local and global. For elastic wave radiation, local conditions such as absorbing boundary conditions based on paraxial approximation of the wave impedance [11] or infinite elements [12] have been developed. Global methods include Boundary Element Methods based on integral formulation of elastodynamics [13] and Dirichlet-to-Neumann methods (DtN) [14] which match the numerical solution in the internal domain to an analytical solution in the external domain. Hybrid finite element-analytical methods have been initially developed in elastodynamics to address the problem of elastic or seismic wave scattering from buried cavities or inclusions. 2D hybrid models in plane strain have been proposed to analyze elastic plane waves scattering from cylindrical cavities in unbounded [15] or half space [16]. The Dirichlet-to-Neumann finite element method has been introduced later to give a more general frame to finite element method for unbounded domain problems [17, 18]. This method requires an analytical expression of the DtN map, which is a nonlocal linear operator, on the artificial boundary. In a subsequent paper, the DtN-finite element method has been extended to 2D elastodynamics in plane strain and in plane stress [19].

In this paper, the hybrid DtN-finite element method is developed for radiation of elastic waves in the rotationally symmetric case on the basis of an analytical series expansion of the external field proposed by Thiruvenkatachar *et al.*[20]. Theoretical developments and coupling with the finite element model are presented in section 2. The radiation of a point force is studied as test example in section 3 to evaluate the accuracy and limitations of the method. Finally, the radiation of a directional piezoelectric double-ended longitudinal vibrator for 4D seismics is analyzed in section 4.

2. Theoretical formulation

A closed solid domain Ω_s containing a piezoelectric subdomain Ω_p and limited by surface (Γ) pointing outwards is considered. Ω_s is surrounded by an infinite homogeneous isotropic elastic medium Ω_∞. In the following, the problem formulation is based on a coupling between the finite element method used to describe physical quantities in Ω_s, and a series expansion [20], to describe elastic wave radiation in Ω_∞. All the variables exhibit an implicit $e^{+j\omega t}$ dependence where ω denotes the angular frequency and t the time.

2.1. Finite element formulation

In Ω_s, the physical quantities of interest are the displacement vector $\boldsymbol{u}$ and the electric potential ψ. The nodal values of $\boldsymbol{u}$ and ψ are the unknowns of the following set of finite element equations [21]

$$\begin{bmatrix} [K_{uu}]_{\Omega\Omega} - \omega^2[M]_{\Omega\Omega} & [K_{uu}]_{\Omega\Gamma} - \omega^2[M]_{\Omega\Gamma} & [K_{u\psi}] \\ \left([K_{uu}]_{\Omega\Gamma} - \omega^2[M]_{\Omega\Gamma}\right)^T & [K_{uu}]_{\Gamma\Gamma} - \omega^2[M]_{\Gamma\Gamma} & [0] \\ [K_{u\psi}]^T & [0] & [K_{\psi\psi}] \end{bmatrix} \cdot \begin{Bmatrix} \boldsymbol{U}_\Omega \\ \boldsymbol{U}_\Gamma \\ \boldsymbol{\psi} \end{Bmatrix} = \begin{Bmatrix} \boldsymbol{F}_\Omega \\ \boldsymbol{F}_\Gamma \\ -\boldsymbol{Q} \end{Bmatrix}, \quad (1)$$

where the subscript Ω applies to nodes inside $\Omega_p \cup \Omega_s$ excluding (Γ), and the subscript Γ applies to nodes on (Γ). $\boldsymbol{\psi}$ (resp. $\boldsymbol{Q}$) is the vector of the nodal values of the electric potential (resp. electrical charge), $\boldsymbol{U}$ (resp. $\boldsymbol{F}$) is the vector of the nodal values of the displacement (resp. force). $[K_{uu}]$, $[K_{u\psi}]$ and $[K_{\psi\psi}]$ are respectively the mechanical, piezoelectric and dielectric stiffness matrices. $[M]$ is the consistent mass matrix. If the radiation from a piezoelectric transducer is considered, energy is provided by the electrical voltage generator. Therefore, $\boldsymbol{F}_\Omega = 0$ (no applied external mechanical force) and either $\boldsymbol{\psi} = \boldsymbol{\psi}_0$ where $\boldsymbol{\psi}_0$ is the driving voltage (for the nodes on the hot electrode) or $\boldsymbol{Q} = 0$ (for the nodes inside Ω_p excluding the hot electrode). As the external medium is elastic, surface displacements $\boldsymbol{U}_\Gamma$ are related to surface forces $\boldsymbol{F}_\Gamma$ by an impedance matrix $[Z]$

$$\boldsymbol{F}_\Gamma = [Z]\boldsymbol{U}_\Gamma. \quad (2)$$

The set of equations (1) combined with equation (2) leads to

$$\begin{bmatrix} [K_{uu}]_{\Omega\Omega} - \omega^2[M]_{\Omega\Omega} & [K_{uu}]_{\Omega\Gamma} - \omega^2[M]_{\Omega\Gamma} & \cdots & [K_{u\psi}] \\ \left([K_{uu}]_{\Omega\Gamma} - \omega^2[M]_{\Omega\Gamma}\right)^T & [K_{uu}]_{\Gamma\Gamma} - \omega^2[M]_{\Gamma\Gamma} - [Z] & \cdots & [0] \\ [K_{u\psi}]^T & [0] & & [K_{\psi\psi}] \end{bmatrix} \cdot \begin{Bmatrix} \boldsymbol{U}_\Omega \\ \boldsymbol{U}_\Gamma \\ \boldsymbol{\psi} \end{Bmatrix} = \begin{Bmatrix} 0 \\ 0 \\ -\boldsymbol{Q} \end{Bmatrix}, \quad (3)$$

calculation of $[Z]$ is described in sections 2.2 and 2.3.

2.2. Radiation from a spherical cavity with prescribed surface tractions

An infinite, elastic, homogeneous and isotropic solid is considered in this section. Density, speed of longitudinal and transverse waves are respectively denoted ρ, α and β; $(O, \boldsymbol{e}_x, \boldsymbol{e}_y, \boldsymbol{e}_z)$ and $(O, \boldsymbol{e}_R, \boldsymbol{e}_\theta, \boldsymbol{e}_\varphi)$ refer to Cartesian and spherical coordinates respectively. A spherical volume of radius a, centered at the origin, is subjected on its surface

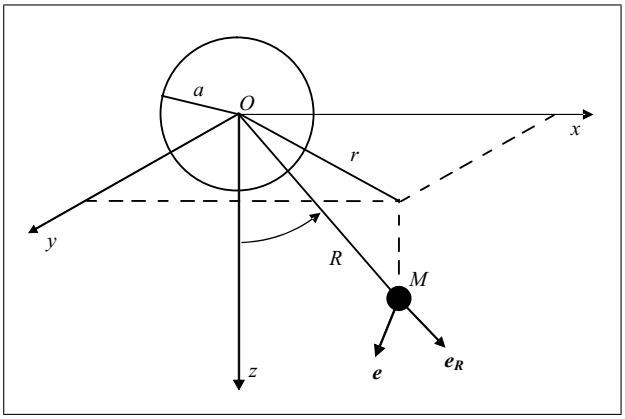

Figure 1. Geometry of the spherical cavity in an infinite medium.

to harmonic time-dependent tractions which are axisymmetrical with respect to O_z (Figure 1). For $R \geq a$, the equation of motion is written as

$$\left[\lambda + \mu\right] \nabla \left\{ \nabla \cdot \boldsymbol{u}(\boldsymbol{M}; \omega) \right\} + \mu \nabla^2 \boldsymbol{u}(\boldsymbol{M}; \omega) = -\rho \omega^2 \boldsymbol{u}(\boldsymbol{M}; \omega), \quad (4)$$

where λ and μ are the Lamé coefficients. The prescribed tractions on the spherical cavity surface are written as

$$\sigma_{RR}(R = a) = f_{RR}(\theta), \quad (5)$$

$$\sigma_{R\theta}(R = a) = f_{R\theta}(\theta). \quad (6)$$

Functions f_{RR} and $f_{R\theta}$ are assumed to be continuous in $[0; \pi]$ and are expressed in terms of series of Legendre polynomials [20]

$$f_{RR}(\theta) = \sum_{n=0}^{\infty} \alpha_n P_n(\cos\theta), \quad (7)$$

$$f_{R\theta}(\theta) = \sum_{n=1}^{\infty} \beta_n \frac{\partial P_n(\cos\theta)}{\partial \theta}. \quad (8)$$

α_n and β_n are series coefficients and P_n is the Legendre polynomial of order n. The general solution of equation (4) is written as

$$\boldsymbol{u}(\boldsymbol{M}; \omega) = \nabla \phi(\boldsymbol{M}; \omega) - \nabla \times \left\{ \nabla \times \boldsymbol{\zeta}(\boldsymbol{M}; \omega) \right\}, \quad (9)$$

where ϕ and $\boldsymbol{\zeta}$ are the scalar and vector generating functions.

Several choices are possible for the shear wave potential. The scalar potential multiplied by $\boldsymbol{e}_R$ is the best choice in an infinite medium [22]. In reference [20], Thiruvenkatachar *et al.* used the scalar potential multiplied by $\boldsymbol{e}_z$ to calculate vector fields in a semi-infinite medium with traction free surface, the infinite medium solution being automatically found as the first term of the development. Thiruvenkatachar development has been chosen and implemented in the finite element code in order to describe both infinite and semi-infinite model in a unique formalism. In this paper, infinite medium is considered and model description is limited to the first term of the development. The vector potential ζ is chosen such as

$$\boldsymbol{\zeta}(\boldsymbol{M}; \omega) = \zeta(\boldsymbol{M}; \omega) \boldsymbol{e}_z. \quad (10)$$

Combining equations (4) and (9), ϕ and ζ are found to be the solutions of the Helmholtz wave equations

$$\nabla^2 \phi(\boldsymbol{M}; \omega) + k_\alpha^2 \phi(\boldsymbol{M}; \omega) = 0, \quad (11)$$

$$\nabla^2 \zeta(\boldsymbol{M}; \omega) + k_\beta^2 \zeta(\boldsymbol{M}; \omega) = 0, \quad (12)$$

where k_α and k_β are respectively the wavenumber of the longitudinal and the transverse waves

$$k_\alpha = \omega / \alpha, \quad (13)$$

$$k_\beta = \omega / \beta. \quad (14)$$

The functions ϕ and ζ which verify equations (11) and (12) are expressed in terms of the following series

$$\phi(\boldsymbol{M}; \omega) = \sum_{n=0}^{\infty} a_n h_n(k_\alpha R) P_n(\cos\theta), \quad (15)$$

$$\zeta(\boldsymbol{M}; \omega) = \sum_{n=0}^{\infty} b_n h_n(k_\beta R) P_n(\cos\theta), \quad (16)$$

where h_n is the spherical Hankel function of the second kind and order n and a_n and b_n are the series coefficients. From equation (9), the spherical polar components of the displacement are written as

$$U_R(\boldsymbol{M}; \omega) = \frac{\partial \phi(\boldsymbol{M}; \omega)}{\partial R} - \frac{1}{R \sin\theta} \cdot \frac{\partial}{\partial \theta} \left[\sin\theta \left\{ - \frac{\partial \zeta(\boldsymbol{M}; \omega)}{\partial r} \right\} \right], \quad (17)$$

$$U_\theta(\boldsymbol{M}; \omega) = \frac{1}{R} \frac{\partial \phi(\boldsymbol{M}; \omega)}{\partial \theta} + \frac{1}{R} \cdot \frac{\partial}{\partial R} \left[R \left\{ - \frac{\partial \zeta(\boldsymbol{M}; \omega)}{\partial r} \right\} \right], \quad (18)$$

$$U_\phi(\boldsymbol{M}; \omega) = 0, \quad (19)$$

where r is the distance between point $\boldsymbol{M}$ and the z-axis (Figure 1). Using properties of both spherical Bessel functions and Legendre polynomials [23], as well as equation (16), the derivative of ζ with respect to r is shown to be written as (see Appendix A1)

$$-\frac{\partial \zeta(\boldsymbol{M}; \omega)}{\partial r} = \sum_{n=1}^{\infty} c_n h_n(k_\beta R) \frac{\partial P_n(\cos\theta)}{\partial \theta}, \quad (20)$$

where

$$c_n = -k_\beta \left[\frac{b_{n+1}}{2n+3} - \frac{b_{n-1}}{2n-1} \right]. \quad (21)$$

$u_R(\boldsymbol{M};\omega)$ and $u_\theta(\boldsymbol{M};\omega)$ are obtained using equations (15) to (21),

$$U_R(\boldsymbol{M};\omega) = \sum_{n=0}^{\infty} a_n g_n^{RR}(k_\alpha R) P_n(\cos\theta) + \sum_{n=1}^{\infty} c_n g_n^{R\theta}(k_\beta R) P_n(\cos\theta), \quad (22)$$

$$U_\theta(\boldsymbol{M};\omega) = \sum_{n=1}^{\infty} \left[c_n g_n^{\theta\theta}(k_\beta R) + a_n g_n^{\theta R}(k_\alpha R) \right] \cdot \frac{\partial P_n(\cos\theta)}{\partial\theta}, \quad (23)$$

where the functions g_n^{RR}, $g_n^{\theta\theta}$, $g_n^{R\theta}$, $g_n^{\theta R}$ are given by

$$g_n^{RR}(k_\alpha R) = k_\alpha h_{n-1}(k_\alpha R) - \frac{[n+1]}{R} h_n(k_\alpha R), \quad (24)$$

$$g_n^{\theta\theta}(k_\beta R) = k_\beta h_{n-1}(k_\beta R) - \frac{n}{R} h_n(k_\beta R), \quad (25)$$

$$g_n^{R\theta}(k_\beta R) = \frac{n[n+1]}{R} h_n(k_\beta R), \quad (26)$$

$$g_n^{\theta R}(k_\alpha R) = \frac{1}{R} h_n(k_\alpha R). \quad (27)$$

Expressions for σ_{RR} and $\sigma_{R\theta}$ are derived by combining equations (22) to (27) with the relations given in Appendix A2 for the stress field calculation. The boundary conditions on (Γ) given by equations (5) and (6) lead to the following set of equations

$$\left.\begin{aligned} A_0(a)a_0 &= \alpha_0, \\ A_n(a)a_n + B_n(a)c_n &= \alpha_n, \\ C_n(a)a_n + D_n(a)c_n &= \beta_n, \end{aligned}\right\} n = 1, 2, 3, \ldots, \quad (28)$$

where

$$A_n(R) = \mu\left[\left(\frac{2[n+1][n+2]}{R^2} - k_\alpha^2\right) h_n(k_\alpha R) - \frac{4k_\alpha}{R} h_{n-1}(k_\alpha R)\right] \quad (29)$$

$$B_n(R) = 2\mu \frac{n[n+1]}{R^2} \left(k_\beta R h_{n-1}(k_\beta R) - [n+2] h_n(k_\beta R)\right), \quad (30)$$

$$C_n(R) = \frac{2\mu}{R^2}\left[k_\alpha R h_{n-1}(k_\alpha R) - [n+2] h_n(k_\alpha R)\right], \quad (31)$$

$$D_n(R) = \mu\left[\left(\frac{2n[n+2]}{R^2} - k_\beta^2\right) h_n(k_\beta R) - \frac{2k_\beta}{R} h_{n-1}(k_\beta R)\right]. \quad (32)$$

Coefficients a_n ($n = 0, 1, 2, \ldots$) and c_n ($n = 1, 2, \ldots$) are calculated by solving the system of equations (28).

2.3. Impedance matrix

The impedance matrix represents the discretized interrelation between the nodal forces and the nodal displacements on (Γ). Starting from the continuous formulation presented in the previous section, the discretization is obtained by considering firstly the relationship between the applied stress field and the nodal displacements, and secondly the relationship between the applied stress field and the nodal forces.

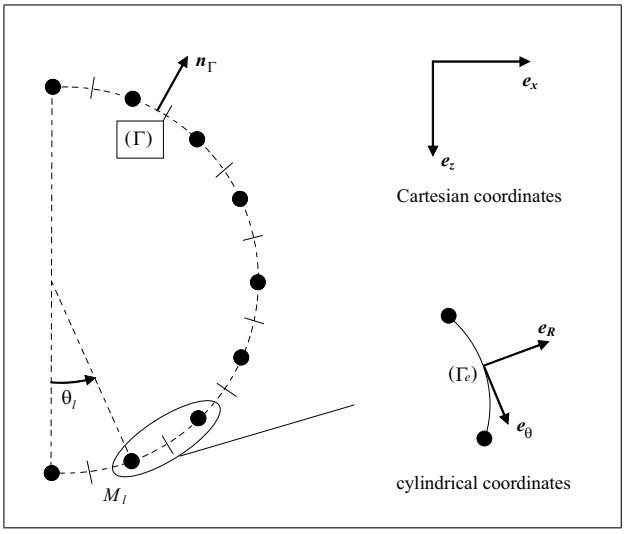

Figure 2. Mesh of the surface of the spherical cavity - spherical and Cartesian coordinates system.

Let us consider a mesh of the surface of the spherical cavity, made of M quadratic three-noded elements connected at nodes $M_l(a, \theta_l)$ ($0 \le \theta_l \le \pi$, $1 \le l \le N = 2M+1$) (Figure 2). From equations (5) to (8), the surface force density Σ_Γ on (Γ) is written in a matrix form

$$\Sigma_\Gamma(\theta) = \begin{Bmatrix} \sigma_{RR}(\theta) \\ \sigma_{R\theta}(\theta) \end{Bmatrix} = \left[L(\theta)\right] \boldsymbol{A}_\Gamma, \quad (33)$$

$$\left[L\right] = \begin{bmatrix} P_0(\cos\theta) & 0 & \cdots \\ 0 & \frac{\partial P_1(\cos\theta)}{\partial\theta} & \cdots \\ \cdots & P_{N-2}(\cos\theta) & 0 \\ \cdots & 0 & \frac{\partial P_{N-1}(\cos\theta)}{\partial\theta} \end{bmatrix}, \quad (34)$$

$$\boldsymbol{A}_\Gamma = \begin{Bmatrix} \alpha_0 & \beta_1 & \cdots & \alpha_{n-2} & \beta_{N-1} \end{Bmatrix}^T. \quad (35)$$

In the Cartesian coordinate system, the surface force density $\boldsymbol{f}_\Gamma$ is written as

$$\boldsymbol{f}_\Gamma = \left[P(\theta)\right] \Sigma_\Gamma(\theta), \quad (36)$$

where the matrix $[P(\theta)]$ is defined by

$$\left[P(\theta)\right] = \begin{bmatrix} -\cos\theta & \sin\theta \\ \sin\theta & \cos\theta \end{bmatrix}. \quad (37)$$

The vector of nodal displacement $\boldsymbol{U}_\Gamma$ is composed of $2N-2$ components since the tangential component vanishes for nodes M_1 and M_N

$$\boldsymbol{U}_\Gamma = \begin{Bmatrix} U_x(\theta_1 = 0) & U_x(\theta_2) & U_y(\theta_2) & \cdots & U_x(\theta_{N-1}) & U_y(\theta_{N-1}) & U_x(\theta_N = \pi) \end{Bmatrix}. \quad (38)$$

Considering the properties of the interpolation functions [24], the value of the displacement at M_l is equal to the nodal value of displacement at M_l. Let us consider a prescribed surface force density $\boldsymbol{f}_\Gamma^i$ $(1 \le i \le 2N-2)$ corresponding to a single term of the series development with a unit coefficient

$$\boldsymbol{f}_\Gamma^i = \left[P(\theta)\right]\left[L(\theta)\right]A_\Gamma^i, \tag{39}$$

with

$$A_\Gamma^i = \left\{0 \ \cdots \ 0 \ \underset{\text{column } i}{1} \ 0 \ \cdots \ 0\right\}^T. \tag{40}$$

The vector of the nodal values of displacements $\boldsymbol{U}_\Gamma^i$, produced by surface force density $\boldsymbol{f}_\Gamma^i$, is calculated using the method presented in section 1.2. By assembling the nodal displacement vectors for all the terms of the series development with unit coefficients, the matrix

$$\left[T_U\right] = \left[U_\Gamma^1 \ U_\Gamma^2 \ \cdots \ U_\Gamma^{2N-2}\right] \tag{41}$$

is built. For an arbitrary surface force density $\boldsymbol{f}_\Gamma$ (and associated vector $\boldsymbol{A}_\Gamma$), vector $\boldsymbol{U}_\Gamma$ is therefore given by

$$\boldsymbol{U}_\Gamma = \left[T_U\right]\boldsymbol{A}_\Gamma. \tag{42}$$

The relationship between the applied stress field and the nodal forces is now considered. In the Cartesian coordinate system, vector $\boldsymbol{F}_\Gamma$ containing the nodal values of the forces equivalent to a stress field is derived from the principle of the virtual works [24, 25]. Considering the stress field $\overline{\overline{\sigma}}^e$ applied on element e with surface (Γ^e) pointing outwards (see Figure 2) and a virtual displacement $\boldsymbol{u}^e$ given by

$$\boldsymbol{u}^e = \left[N^e\right]\boldsymbol{U}_\Gamma^e, \tag{43}$$

where $[N^e]$ is the matrix of the shape functions associated with finite element e, the principle of virtual works is written as

$$\iint_{(\Gamma^e)} \boldsymbol{u}^{eT}\overline{\overline{\sigma}}^e\,\boldsymbol{n}_\Gamma\,\mathrm{d}\Gamma = \left\{\boldsymbol{U}_\Gamma^e\right\}^T\boldsymbol{F}_\Gamma^e. \tag{44}$$

$\boldsymbol{U}_\Gamma^e$ (resp. $\boldsymbol{F}_\Gamma^e$) are the vectors of the nodal values of displacements (resp. forces) for element e. Combining equations (43) and (44), vector $\boldsymbol{F}_\Gamma^e$ is obtained by identification,

$$\boldsymbol{F}_\Gamma^e = \iint_{(\Gamma^e)} \left[n^e\right]^T\overline{\overline{\sigma}}^e\,\boldsymbol{n}_\Gamma\,\mathrm{d}\Gamma. \tag{45}$$

Considering the surface force density $\boldsymbol{f}_\Gamma^e$ on (Γ^e)

$$\overline{\overline{\sigma}}^e\,\boldsymbol{n}_\Gamma = \boldsymbol{f}_\Gamma^e = \left[P(\theta)\right]\left[L(\theta)\right]\boldsymbol{A}_\Gamma, \tag{46}$$

equation (39) is written as

$$\boldsymbol{F}_\Gamma^e = \left[T_F^e\right]\boldsymbol{A}_\Gamma, \tag{47}$$

with

$$\left[T_F^e\right] = \iint_{(\Gamma^e)} \left[N^e\right]^T\left[P(\theta)\right]\left[L(\theta)\right]\mathrm{d}\Gamma. \tag{48}$$

The assembling of elementary vectors expressed by equation (47) gives the relationship between the series coefficient (of the surface force density decomposition) and the nodal forces:

$$F_\Gamma = \left[T_F\right]A_\Gamma. \tag{49}$$

The impedance matrix $[Z]$ is obtained by combining equations (42) and (49),

$$\left[Z\right] = \left[T_F\right]\left[T_u\right]^{-1}. \tag{50}$$

2.4. Displacement field in the infinite elastic medium

If $\boldsymbol{U}_\Gamma$ is known, coefficients a_n and c_n are calculated by writing equations (22) and (23) for each node on (Γ) in a matrix form,

$$\left[G\right]\boldsymbol{C} = \boldsymbol{U}_\Gamma, \tag{51}$$

where vector $\boldsymbol{C}$ is defined by

$$\boldsymbol{C} = \left\{a_0 \ \cdots \ a_{N-1} \ c_1 \ \cdots \ c_{N-2}\right\}^T, \tag{52}$$

and matrix $[G]$ by

$$\left[G\right] = \begin{bmatrix}[G^{RR}] & [G^{R\theta}]\\ [G^{\theta R}] & [G^{\theta\theta}]\end{bmatrix}, \tag{53}$$

with

$$G_{kl}^{RR} = g_{k-l}^{RR}(k_\alpha a)P_{k-l}(\cos\theta_l), \quad \begin{cases}1 \le k \le N,\\ 1 \le l \le N,\end{cases} \tag{54}$$

$$G_{kl}^{\theta\theta} = g_k^{\theta\theta}(k_\beta a)\frac{\partial P_k}{\partial\theta}(\cos\theta_{l+1}), \quad \begin{cases}1 \le k \le N-2,\\ 1 \le l \le N-2,\end{cases} \tag{55}$$

$$G_{kl}^{R\theta} = g_k^{R\theta}(k_\beta a)P_k(\cos\theta_l), \quad \begin{cases}1 \le k \le N-2,\\ 1 \le l \le N,\end{cases} \tag{56}$$

$$G_{kl}^{\theta R} = \delta_{l,k}\delta_{N,k}g_{k-l}^{\theta R}(k_\alpha a)P_{k-l}(\cos\theta_{l+1}), \quad \begin{cases}1 \le k \le N,\\ 1 \le l \le N.\end{cases} \tag{57}$$

$\delta_{l,k}$ denotes the Kronecker symbol. Coefficients a_n and c_n are obtained by inverting the system of equations (51)

$$\boldsymbol{C} = \left[G\right]^{-1}\boldsymbol{U}_\Gamma. \tag{58}$$

2.5. Implementation

The theoretical formulation described in the previous sections is implemented in the finite element code ATILA [26]. Specific surface elements are superposed on the finite element mesh to discretize surface (Γ). The problem is solved in 4 steps:

(i) Computation of the standard finite element stiffness and mass matrices;
(ii) Computation of the impedance matrix on (Γ) (equation (50));
(iii) Resolution of matrix equation (3);
(iv) Computation of displacement in Ω_∞ (equations (22), (23) and (58)).

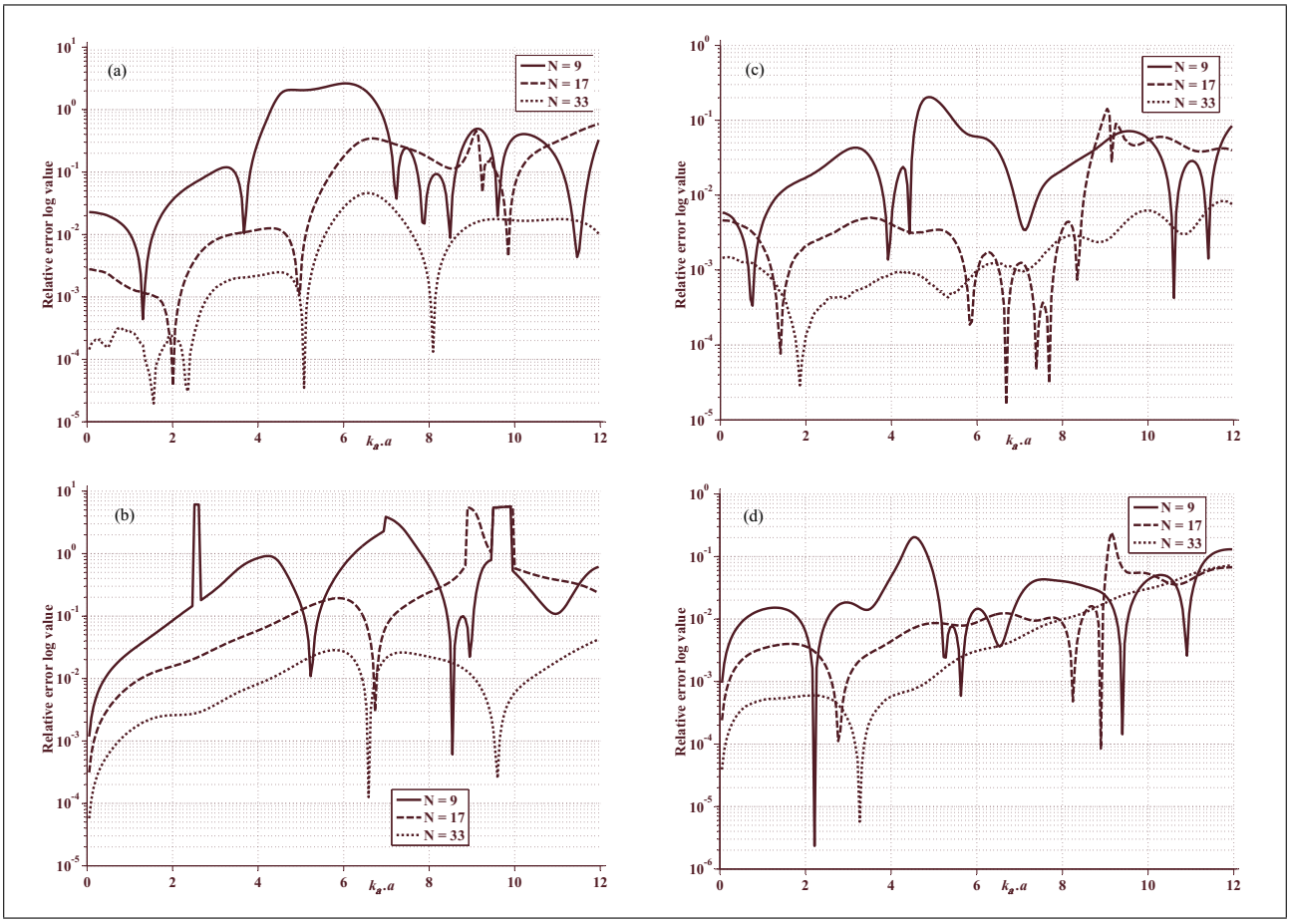

Figure 3. Point force acting in the infinite elastic medium. Relative error on numerically computed displacement on the mesh boundary. N is the number of terms in the series development. $R = a$, $\theta = 0$ (a) radial displacement modulus, (b) radial displacement phase. $R = a$, $\theta = \pi/2$ (c) tangential displacement modulus, (d) tangential displacement phase.

3. Test example: The point force

The point force $\boldsymbol{F} = \boldsymbol{F}_0 \mathrm{e}^{+\mathrm{j}\omega t}\boldsymbol{e}_z$ acting in an infinite elastic isotropic homogeneous medium is considered as a test example. This problem has an analytical solution [27] expressed in spherical coordinates

$$u_R^f(\boldsymbol{M};\omega) = \frac{F_0 \cos\theta}{4\pi\rho\omega^2}\left[2\left[\frac{\mathrm{e}^{-\mathrm{j}k_\beta R} - \mathrm{e}^{-\mathrm{j}k_\alpha R}}{R^3} - \mathrm{j}\frac{k_\beta \mathrm{e}^{-\mathrm{j}k_\beta R} - k_\alpha \mathrm{e}^{-\mathrm{j}k_\alpha R}}{R^2}\right] + \frac{k_\alpha^2 \mathrm{e}^{-\mathrm{j}k_\alpha R}}{R}\right], \quad (59)$$

$$u_\theta^f(\boldsymbol{M};\omega) = \frac{F_0 \sin\theta}{4\pi\rho\omega^2}\left[\left[\frac{\mathrm{e}^{-\mathrm{j}k_\beta R} - \mathrm{e}^{-\mathrm{j}k_\alpha R}}{R^3} - \mathrm{j}\frac{k_\beta \mathrm{e}^{-\mathrm{j}k_\beta R} - k_\alpha \mathrm{e}^{-\mathrm{j}k_\alpha R}}{R^2}\right] - \frac{k_\beta^2 \mathrm{e}^{-\mathrm{j}k_\beta R}}{R}\right], \quad (60)$$

and $u_\phi^f(\boldsymbol{M};\omega) = 0$. In the axisymmetrical finite element model, the spherical volume Ω_s is meshed by quadratic 6-noded triangular and 8-noded quadrilateral elements, the point force being applied at the central node of the spherical volume. Surface (Γ) is meshed by quadratic 3-node elements. It is not possible to model exactly a point force with a finite element model as the spatial distribution of the force is described by the interpolation functions of the neighboring elements. Therefore, a high density mesh is used around the central node in order to have a force distribution which is similar to a point force. Further from the source, larger elements having a constant size along e_R are used. The physical constants of the medium are $\rho = 3300\,\mathrm{kg/m^3}$, $\alpha = 2500\,\mathrm{m/s}$ and $\beta = \alpha/\sqrt{3}$. The reduced frequency $k_\alpha a$ varies from 0.05 to 12, a being the radius of the spherical volume Ω_s. The usual finite element cut-off reduced frequency (for which the quadratic element size in the radial direction is equal to one-quarter of wavelength of the transverse wave) is $k_\alpha a = k_\beta/\sqrt{3} \approx 10.9$.

The relative error on displacement modulus and phase, $\varepsilon_p^{\mathrm{mod}}(R,\theta;\omega)$ and $\varepsilon_p^{\mathrm{pha}}(R,\theta;\omega)$, are defined as

$$\varepsilon_p^{\mathrm{mod}}(R,\theta;\omega) = \left|\frac{\left|u_p(R,\theta;\omega)\right| - \left|u_p^f(R,\theta;\omega)\right|}{\left|u_p^f(R,\theta;\omega)\right|}\right|, \quad (61)$$

$$\varepsilon_p^{\mathrm{pha}}(R,\theta;\omega) = \left|\frac{\mathrm{Arg}\left[u_p(R,\theta;\omega)\right] - \mathrm{Arg}\left[u_p^f(R,\theta;\omega)\right]}{\mathrm{Arg}\left[u_p^f(R,\theta;\omega)\right]}\right|, \quad (62)$$

where u_p is the numerically computed displacement, p denoting R or θ. These relative errors are displayed in Figures 3 and 4 for various numbers of terms in the series

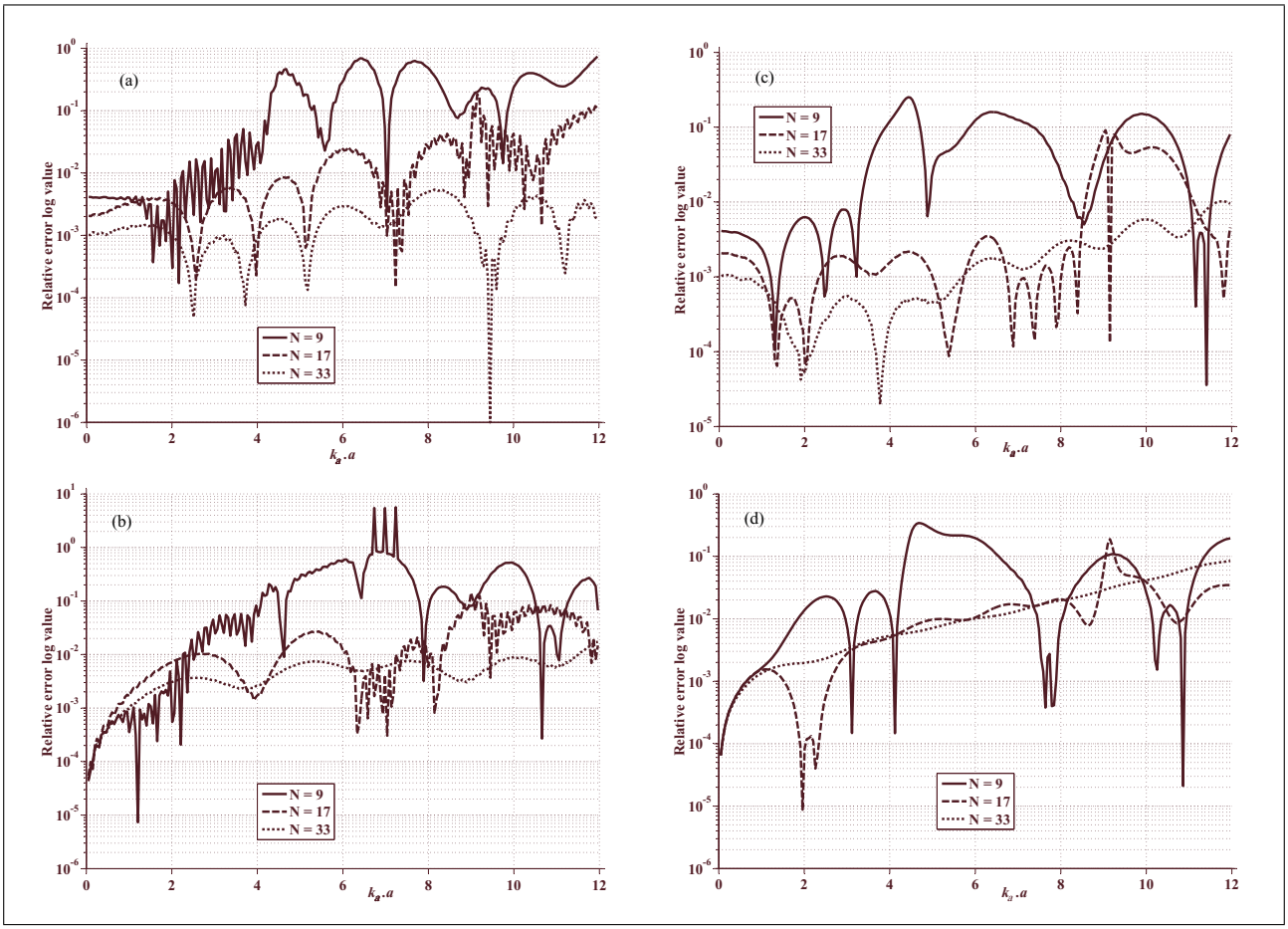

Figure 4. Point force acting in the infinite elastic medium. Relative error on numerically computed displacement in the far-field. N is the number of terms in the series development. $R = 50a$, $\theta = 0$ (a) radial displacement modulus, (b) radial displacement phase. $R = 50a$, $\theta = \pi/2$ (c) tangential displacement modulus, (d) tangential displacement phase.

Table I. Point force acting in the infinite elastic medium. Upper reduced frequencies $k_\alpha d$ corresponding to 3% relative error on displacement modulus.

	$N = 9$	$N = 17$	$N = 33$
$R = a, \theta = 0$	1.87	5.31	6.02
$R = a, \theta = \pi/2$	2.59	8.54	>12
$R = 50a, \theta = 0$	3.31	8.07	>12
$R = 50a, \theta = \pi/2$	3.46	8.74	>12

Table II. Point force acting in the infinite elastic medium. Upper reduced frequencies $k_\alpha d$ corresponding to 3% relative error on displacement phase.

	$N = 9$	$N = 17$	$N = 33$
$R = a, \theta = 0$	1.06	2.96	11.43
$R = a, \theta = \pi/2$	3.83	8.96	9.88
$R = 50a, \theta = 0$	2.74	8.47	>12
$R = 50a, \theta = \pi/2$	4.25	8.79	9.01

expansion ($N = 9$, 17 and 33) at four characteristic points located on surface (Γ) ($R = a$) and in Ω_∞ ($R = 50a$). The upper frequencies corresponding to a 3% relative error on amplitude or phase are displayed in Tables I and II. It can be noted that

i) For any N, the general trend shows an error increase with frequency. Therefore, the coupled method can be considered as a "low frequency" method well-suited to seismic applications.

ii) For all cases, the error is related to N and decreases in the whole frequency range when N increases. It is larger than the usual error associated to a finite element discretization.

iii) The error is larger at $R = a$, as the near-field terms in (59) and (60) lead to a more complicated displacement field than in the far-field.

4. Application example: The directional double-ended piezoelectric longitudinal vibrator

4.1. Ideal directional source

An ideal directional source is obtained by combining the point force and the couple of forces with moment with ad-

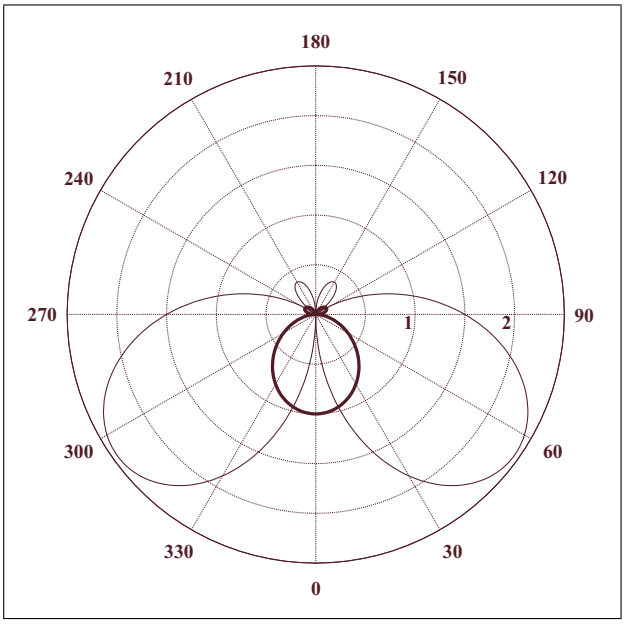

Figure 5. Far-field radiated displacement patterns of a directional point force-couple of forces combination. Thick line: radial displacement; thin line: tangential displacement.

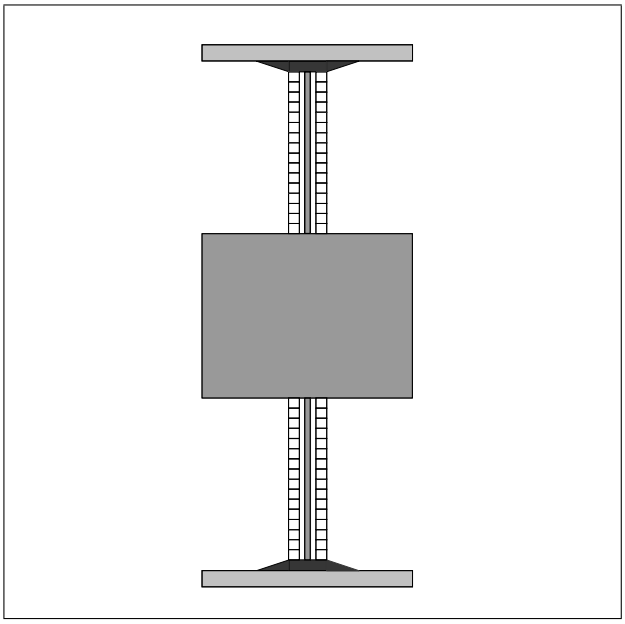

Figure 6. Geometry of the piezoelectric double-ended longitudinal vibrator.

equate amplitudes and phases. The analytical expression for the far-field displacement $\boldsymbol{u}^c$ generated by a couple of forces without moment ($-\boldsymbol{F}'_0 \mathrm{e}^{+\mathrm{j}\omega t}\boldsymbol{e}_z$ acting in A and $\boldsymbol{F}'_0 \mathrm{e}^{+\mathrm{j}\omega t}\boldsymbol{e}_z$ acting in A' with $\boldsymbol{A'O} = \boldsymbol{OA} = d\boldsymbol{e}_z$) is in the low frequency approximation [27]:

$$u_R^c(\boldsymbol{M};\omega) = \frac{\mathrm{j}F'_0 d k_\alpha^3 \cos^2\theta}{2\pi\rho\omega^2}\frac{\mathrm{e}^{-\mathrm{j}k_\alpha R}}{R}, \tag{63}$$

$$u_\theta^c(\boldsymbol{M};\omega) = -\frac{\mathrm{j}F'_0 d k_\beta^3 \sin\theta\cos\theta}{2\pi\rho\omega^2}\frac{\mathrm{e}^{-\mathrm{j}k_\beta R}}{R}, \tag{64}$$

and $u_\phi^c(\boldsymbol{M};\omega) = 0$. The combination of the point force and the couple of forces generates a far-field displacement $\boldsymbol{u}^{\mathrm{comb}}$ obtained by adding far-field terms of equations (63) and (64):

$$u_R^{\mathrm{comb}}(\boldsymbol{M};\omega) = \frac{k_\alpha^2 \cos\theta\left[F_0 + 2\mathrm{j}F'_0 k_\alpha d\cos\theta\right]}{4\pi\rho\omega^2}\frac{\mathrm{e}^{-\mathrm{j}k_\alpha R}}{R}, \tag{65}$$

$$u_\theta^{\mathrm{comb}}(\boldsymbol{M};\omega) = -\frac{k_\beta^2 \sin\theta\left[F_0 + 2\mathrm{j}F'_0 k_\beta d\cos\theta\right]}{4\pi\rho\omega^2}\frac{\mathrm{e}^{-\mathrm{j}k_\beta R}}{R}, \tag{66}$$

In previous works [6, 7, 28], it has been demonstrated that equations (65) and (66) can lead to directional far-field radiation for both longitudinal and transverse waves if F_0 and F'_0 are adequately chosen. Thus, the combination of the point force and the couple of forces which verifies

$$F_0 = -2\mathrm{j}F'_0 k_\alpha d, \tag{67}$$

theoretically cancels the far-field radiation of the longitudinal wave along $\theta = \pi$ (equation 65). Figure 5 shows that, in that case, a directional far-field radiation is also obtained for transverse waves.

4.2. Directional doubled-ended piezoelectric vibrator

The aim of the present model is to determine if such a directional radiation can be obtained with the piezoelectric

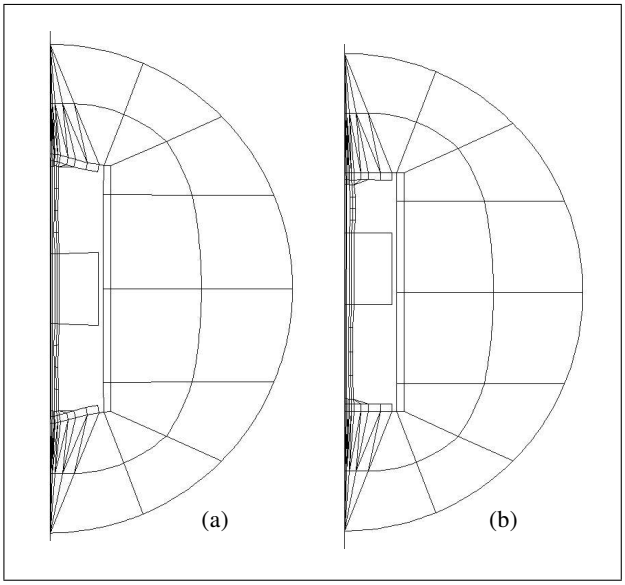

Figure 7. Displacement field of the piezoelectric double-ended longitudinal vibrator at $k_\alpha d = 0.25$. (a) stacks driven with identical amplitudes and phases. (b) stacks driven with identical amplitudes and opposite phases.

double-ended longitudinal vibrator. The transducer consists of two ceramic stacks mounted between a steel-made central tail-mass and aluminum end-masses (Figure 6). It is mounted in a steel-made cylindrical baffle (height d, radius $d/4$, thickness $d/20$) and surrounded by infinite elastic isotropic homogeneous formation (physical constants given in section 3). When the stacks are driven with electrical voltages of identical amplitudes but opposite phases, an anti-symmetrical vibration is generated with respect to the central tail-mass. In the low frequency approximation ($k_\alpha d \ll 2\pi$, $k_\beta d \ll 2\pi$), the transducer with anti-

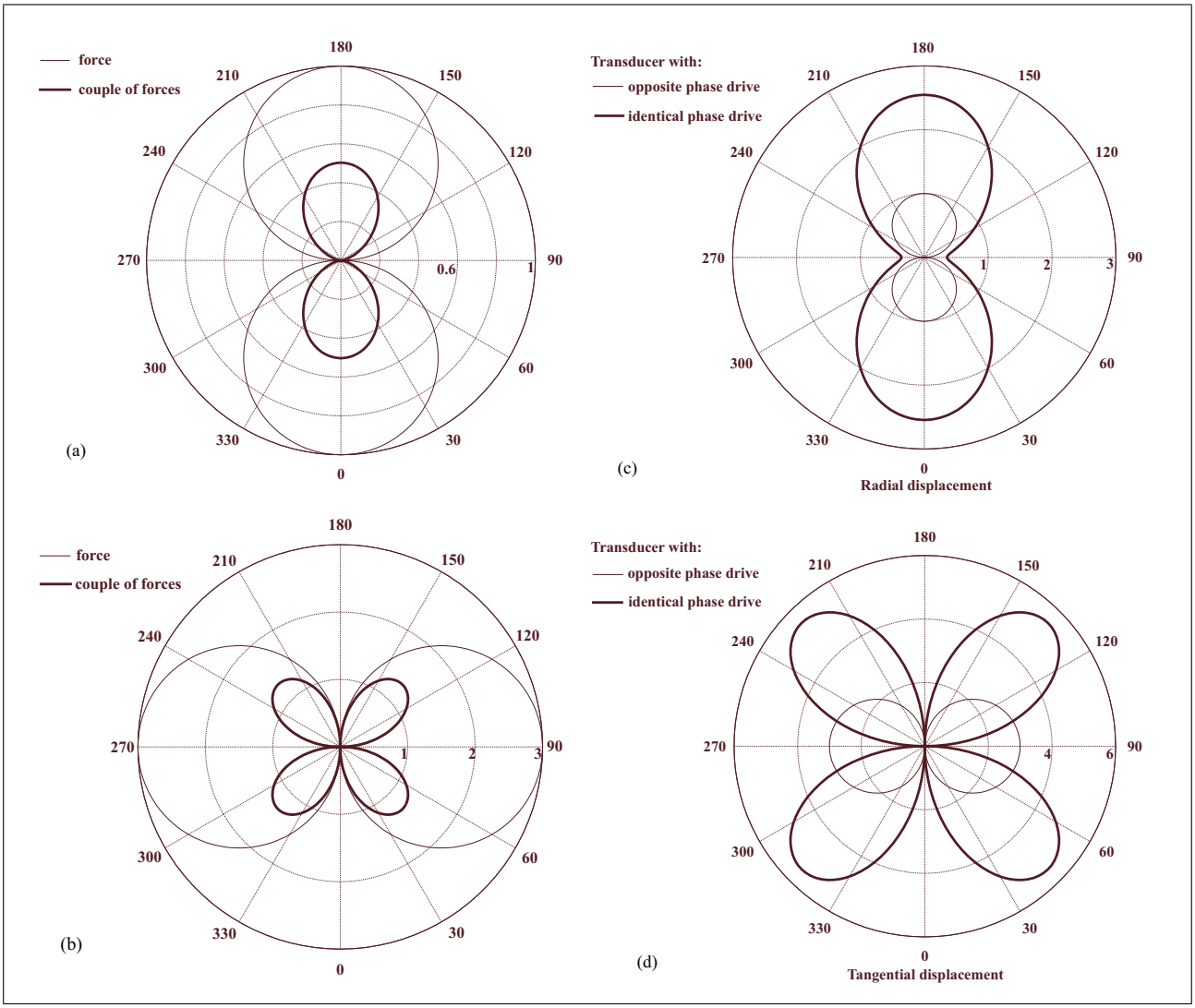

Figure 8. Far-field radiated displacement patterns. Ideal point force (thin line) and couple of forces (thick line): (a) radial displacement, (b) tangential displacement. Piezoelectric double-ended longitudinal vibrator with symmetrical (thick line) and anti-symmetrical (thin line), displacement at $R = 2000d$ and $k_\alpha d = 0.25$: (c) radial displacement, (d) tangential displacement.

symmetrical vibration can be considered as a point force. When the stacks are driven with electrical voltages of identical amplitudes and phases, a symmetrical vibration is generated and the transducer acts as a couple of forces without moment.

The numerical computation of the double-ended longitudinal vibrator is performed with $N = 17$ and $N = 41$ to check convergence of the results. Figure 7 displays the computed transducer displacement field at $k_\alpha d = 0.25$ for symmetrical and anti-symmetrical electrical drives. As the frequency of computation is much lower than the lowest resonance frequency of the transducer, the vibration is mainly dominated by stiffness effects. When driven in phase (Figure 7a), both ceramic stacks vibrate in phase and the transducer behaves as a couple of forces. The central mass is almost motionless as the symmetry plane is a node of vibration. The maximum amplitude of vibration is observed at the end-masses which display a strong flexure. When driven with opposite phases (Figure 7b), an anti-symmetrical motion of the transducer is generated. The central-mass undergoes a much larger longitudinal motion than the end- masses as the compliance of the formation is much smaller than the compliance of the ceramic stacks. Figure 8 compares the computed transducer far-field directivity patterns to those of ideal point force and couple of forces at $k_\alpha d = 0.25$. When considering separately the couple of forces and the transducer with in-phase drives on one hand, and the point force and the transducer with out-of-phase drive on the other hand, a good agreement is obtained between directivity patterns. However, the ratio of force to couple of forces displacement amplitude is 5 times larger in the ideal source case than in the transducer case, due to the variation of effective transducer compliance between symmetrical and anti-symmetrical vibrations.

If the compliance of the transducer is neglected, the acting force of each end-mass is proportional to the voltage applied to the stack

$$F_u = A\Phi_u = -F_0'/2 + F_0/2, \quad F_l = A\Phi_l = F_0'/2 + F_0/2, \quad (68)$$

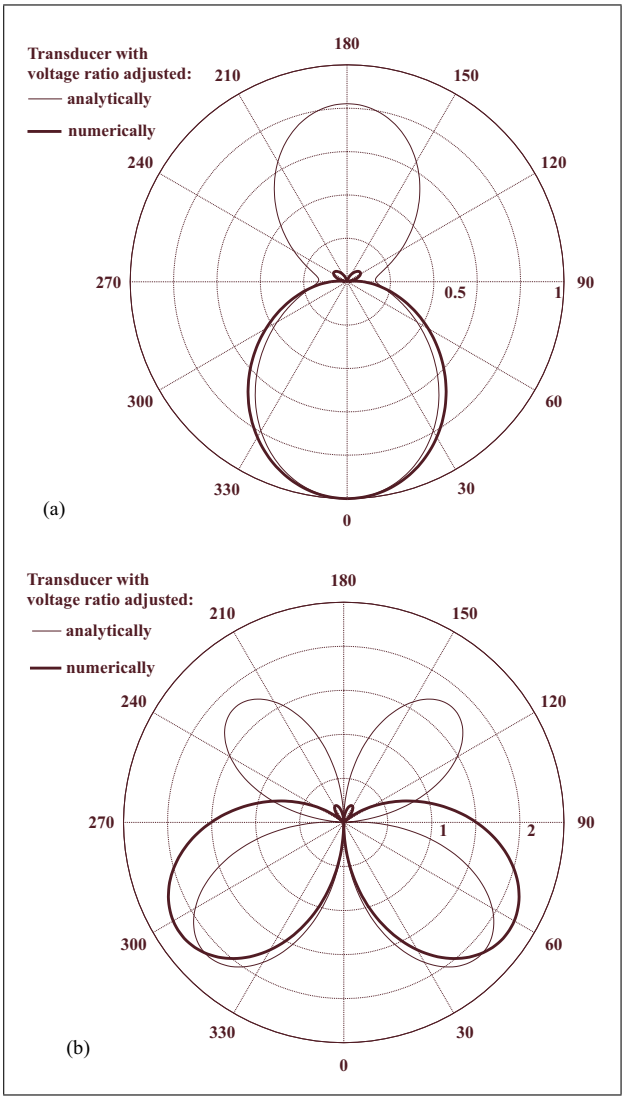

Figure 9. Directional radiated displacement patterns at $R = 2000d$ and $k_\alpha d = 0.25$. Piezoelectric double-ended longitudinal vibrator with analytically (thin line) and numerically (thick line) adjusted drives. (a) radial displacement, (b) tangential displacement.

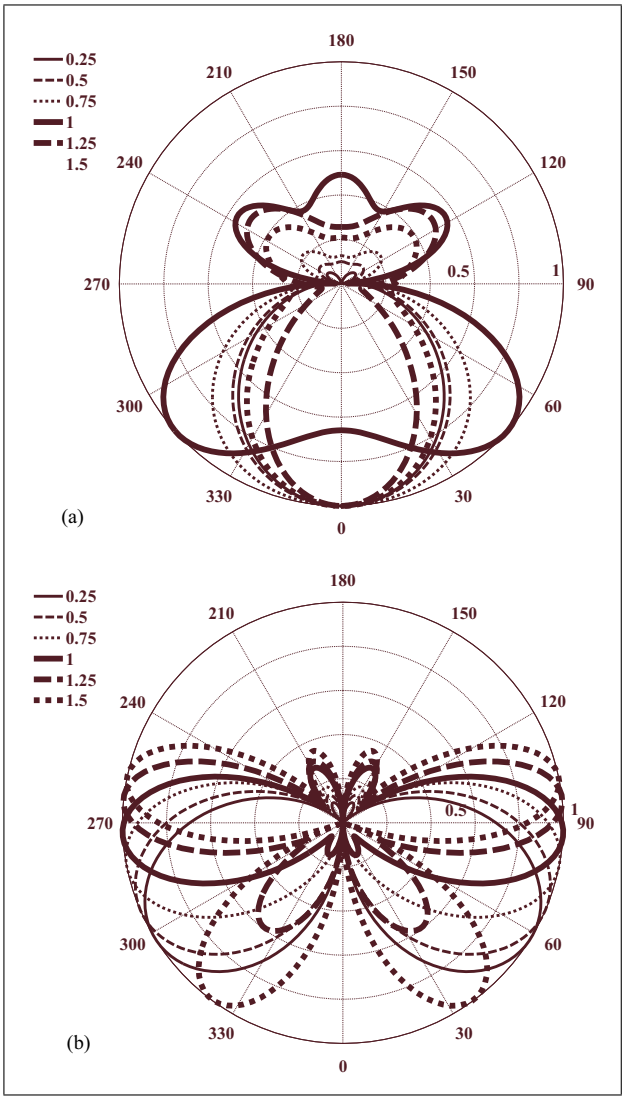

Figure 10. Directional radiated displacement patterns at $R = 2000d$ of the piezoelectric double-ended longitudinal vibrator with numerically adjusted drive for various kad values. (a) radial displacement, (b) tangential displacement.

where subscripts u and l denote the upper and lower stacks (or end-masses) respectively. By combining equations (67) and (68), the theoretical condition for a directional radiation of the transducer is written as:

$$\Phi_u = -\left[\frac{1 - jk_\alpha d}{1 + jk_\alpha d}\right]\Phi_l. \tag{69}$$

The computed far-field directivity patterns at $k_\alpha d = 0.25$ (Figure 9), with applied voltages verifying equation (69), show that the directional radiation is not obtained, due to the aforementioned difference in amplitude ratio. To avoid this problem, the ratio Φ_u/Φ_l that cancels the far-field radiation of the longitudinal wave along $\theta = \pi$ is extracted from numerical computation with opposite and identical phase electrical drives. When using this numerically computed voltage ratio, a directional radiation from the transducer is obtained for both longitudinal and transverse waves at $k_\alpha d = 0.25$ (Figure 9) and at higher frequencies (Figure 10).

5. Conclusion

A numerical method is developed to describe, in the frequency domain, the elastic waves radiated from a piezoelectric transducer in an infinite elastic medium. This method relies upon the coupling between the Finite Element Method (to model the transducer and the surrounding medium up to a spherical boundary) and a series expansion (to model the field on and outside the boundary). Validation tests conducted on the point force show that the accuracy of the results is mainly determined by the number of terms used in the series expansion which has to be increased when the frequency increases. This coupled method is a "low frequency" method as higher

computational efficiency and accuracy are obtained when the source size is small compared to the wavelength. It is therefore well-suited to seismic applications.

The design of a directional piezoelectric double-ended longitudinal vibrator for 4D seismic monitoring is considered as an application example. It is based on the combination of the symmetrical vibration of the transducer which acts as a couple of forces, and the anti-symmetrical vibration of the transducer which acts as a force. The voltage amplitude and phase applied on each piezoelectric stack is adjusted to obtain the directional radiation. It is found that the effective transducer compliance strongly affects the relative amplitude of the (symmetrical and anti-symmetrical) modes of vibration and that the control law on voltage must be extracted from the numerical computation to obtain a directional radiation for both longitudinal and transverse waves.

Appendix

A1. Derivation of the vector potential with respect to *r*

Considering the classical relationship

$$\frac{\partial}{\partial r} \equiv \sin\theta \frac{\partial}{\partial R} + \frac{\cos\theta}{R}\frac{\partial}{\partial \theta}, \tag{A1}$$

the derivative of ζ with respect to r is written as

$$\frac{\partial \zeta}{\partial r} = \sum_{n=0}^{+\infty} \Big[\sin\theta \frac{\partial}{\partial R}\left\{b_n h_n(k_\beta R)\right\} P_n(\cos\theta) + \frac{\cos\theta}{R}\frac{\partial}{\partial R}\left\{b_n h_n(k_\beta R)\right\}\frac{\partial P_n(\cos\theta)}{\partial\theta}\Big]. \tag{A2}$$

Using equations (10.1.19) and (10.1.20) of reference [23]:

$$\frac{\partial}{\partial R} h_n(k_\beta R) = k_\beta \Big[\frac{n}{2n+1} h_{n-1}(k_\beta R) - \frac{n+1}{2n+1} h_{n+1}(k_\beta R)\Big], \tag{A3}$$

$$\frac{h_n(k_\beta R)}{R} = k_\beta \Big[\frac{1}{2n+1} h_{n-1}(k_\beta R) + \frac{1}{2n+1} h_{n+1}(k_\beta R)\Big], \tag{A4}$$

(A2) is written

$$\frac{\partial \zeta}{\partial r} = U + V, \tag{A5}$$

$$U = \sum_{n=0}^{+\infty} \frac{b_n}{2n+1}\Big[n \sin\theta P_n(\cos\theta) + \cos\theta \frac{\partial P_n(\cos\theta)}{\partial\theta}\Big] h_{n-1}(k_\beta R), \tag{A6}$$

$$V = \sum_{n=0}^{+\infty} \frac{b_n}{2n+1}\Big[-[n+1]\sin\theta P_n(\cos\theta) + \cos\theta \frac{\partial P_n(\cos\theta)}{\partial\theta}\Big] h_{n+1}(k_\beta R). \tag{A7}$$

$N = n-1$ (resp. $N = n+1$) is introduced in U (resp. in V) to give

$$U = \sum_{n=-1}^{+\infty} \frac{b_{N+1}}{2N+3}\Big[[N+1]\sin\theta P_{N+1}(\cos\theta) + \cos\theta \frac{\partial P_{N+1}(\cos\theta)}{\partial\theta}\Big] h_N(k_\beta R), \tag{A8}$$

$$V = \sum_{n=1}^{+\infty} \frac{b_{N-1}}{2N-1}\Big[-N\sin\theta P_{N-1}\cos\theta) + \cos\theta \frac{\partial P_{N-1}(\cos\theta)}{\partial\theta}\Big] h_N(k_\beta R). \tag{A9}$$

The terms $N = -1$ and $N = 0$ vanish in equation (A8) and U is written as

$$U = \sum_{n=1}^{+\infty} \frac{b_{N+1}}{2N+3}\Big[[N+1]\sin\theta P_{N+1}(\cos\theta) + \cos\theta \frac{\partial P_{N+1}(\cos\theta)}{\partial\theta}\Big] h_N(k_\beta R). \tag{A10}$$

Let us introduce the following quantities in equations (A9) and (A10):

$$W = [N+1]\sin\theta P_{N+1}(\cos\theta) + \cos\theta \frac{\partial P_{N+1}(\cos\theta)}{\partial\theta} \tag{A11}$$

$$Z = -N\sin\theta P_{N-1}(\cos\theta) + \cos\theta \frac{\partial P_{N-1}(\cos\theta)}{\partial\theta}. \tag{A12}$$

Using equation (22.7.10) and (22.8.10) of reference [23], the following relations are derived:

$$-\sin\theta \frac{\partial P_n(\cos\theta)}{\partial\theta} = -n\cos\theta P_n(\cos\theta) + nP_{n-1}(\cos\theta), \tag{A13}$$

$$[n+1]P_{n+1}(\cos\theta) = [2n+1]\cos\theta P_n(\cos\theta) - nP_{n-1}(\cos\theta). \tag{A14}$$

W is transformed by successively combining (A11) and (A13)

$$W = (N+1)\Big[+\frac{1}{sin\theta} P_{N+1}(\cos\theta) - \frac{\cos\theta}{\sin\theta} P_N(\cos\theta)\Big], \tag{A15}$$

(A14) and (A15),

$$W = N\frac{\cos\theta}{\sin\theta} P_N(\cos\theta) - N\frac{1}{sin\theta} P_{N-1}(\cos\theta); \tag{A16}$$

and finally (A13) and (A16)

$$W = \frac{\partial P_N(\cos\theta)}{\partial\theta}. \tag{A17}$$

(A13) and (A14) are combined to give the following relationship,

$$\cos\theta \frac{\partial P_{N-1}(\cos\theta)}{\partial\theta} = -N\frac{\cos^2\theta}{\sin\theta} P_{N-1}(\cos\theta) + N\frac{\cos\theta}{\sin\theta} P_N(\cos\theta). \tag{A18}$$

Z is successively transformed by combining (A12) and (A18)

$$Z = N\frac{\cos\theta}{\sin\theta}P_N(\cos\theta) - N\frac{1}{sin\theta}P_{N-1}(\cos\theta), \qquad \text{(A19)}$$

and (A13) and (A19)

$$Z = \frac{\partial P_N(\cos\theta)}{\partial\theta}. \qquad \text{(A20)}$$

The combination of (A5), (A9) to (A12), A(17) and (A20) finally leads to

$$\frac{\partial\zeta}{\partial r} = \sum_{n=1}^{+\infty} k_\beta\left[\frac{b_{N+1}}{2N+3} + \frac{b_{N-1}}{2N-1}\right] \cdot h_N(k_\beta R)\frac{\partial P_N(\cos\theta)}{\partial\theta}. \qquad \text{(A21)}$$

A2. Stress field in spherical coordinates

In spherical coordinates, components of stress field are written as

$$\sigma_{RR} = \lambda\Theta + 2\mu\frac{\partial u_R}{\partial R}, \qquad \text{(A22)}$$

$$\sigma_{\theta\theta} = \lambda\Theta + 2\mu\left[\frac{1}{R}\frac{\partial u_\theta}{\partial\theta} + \frac{u_R}{R}\right], \qquad \text{(A23)}$$

$$\sigma_{\varphi\varphi} = \lambda\Theta + 2\mu\left[\frac{u_\theta}{R}\text{cotan}\theta + \frac{u_R}{R}\right], \qquad \text{(A24)}$$

$$\sigma_{R\theta} = \mu\left[\frac{\partial u_\theta}{\partial R} + \frac{1}{R}\frac{\partial u_R}{\partial\theta} - \frac{u_\theta}{R}\right], \qquad \text{(A25)}$$

$$\Theta = \frac{1}{R^2\sin\theta}\left[\frac{\partial}{\partial R}\left\{R^2u_R\sin\theta\right\} + \frac{\partial}{\partial\theta}\left\{Ru_\theta\sin\theta\right\}\right]. \qquad \text{(A26)}$$

Other components vanish.

Acknowledgement

This work was supported by Association Nationale de la Recherche Technique (CIFRE grant).

References

[1] R. J. Greaves, T. J. Fulp: Three-dimensional seismic monitoring of an enhanced oil recovery process. Geophysics **52** (1987) 1175–1187.

[2] A. Nur: Four dimensional seismology and (true) direct detection of hydrocarbons: the petrophysical basis. The Leading Edge **8** (1989) 30–36.

[3] J. Eastwood, P. Lebel, A. Dilay, S. Blakeslee: Seismic monitoring of steam-based recovery of bitumen. The Leading Edge **13** (1994) 242–251.

[4] J. P. Castagna, G. Sparkman, B. Gobran: Time lapse reservoir monitoring and characterization. Proc. Workshop of the Energy Research Clearing House, 1996.

[5] J. Meunier, F. Huguet, P. Meynier: Reservoir monitoring using permanent sources and vertical receiver antennae: The Céré-la-Ronde case study. The Leading Edge **20** (2001) 622.

[6] M. Berraki: Theoretical analysis and modelization of a buried directional piezoelectric source for seismic applications (in French). PhD Thesis Dissertation, Université des Sciences et Technologies de Lille, 2004.

[7] M. Berraki, B. Dubus, A. Baroni: Radiation of directional seismic sources within a layered half-space. Proceedings of the Joint Congress CFA-DAGA'04, Strassbourg, 2004, 145–146.

[8] S. C. Butler, A. L. Butler, J. L. Butler: Directional flextensional transducer. J. Acoust. Soc. Am. **92** (1992) 2977–2979.

[9] S. C. Butler, J. L. Butler, A. L. Butler, G. H. Cavanagh: A low-frequency directional flextensional transducer and line array. J. Acoust. Soc. Am. **102** (1997) 308–314.

[10] J. Zhang, A.-C. Hladky-Hennion, W. J. Hughes, E. E. Newnham: A miniature class V flextensional cymbal transducer with directional beam patterns: the double driver. Ultrasonics **39** (2001) 91–95.

[11] D. Givoli: Non-reflecting boundary conditions: a review. J. Comput. Phys. **94** (1991) 1–29.

[12] F. Medina, R. L. Taylor: Infinite elements for elastodynamics. Earthquake Engng Struct. Dyn. **10** (1982) 699–709.

[13] C. A. Brebbia: The boundary element method for engineers. John Wiley and Sons, 1978.

[14] D. Givoli: Recent advances in the DtN FE method. Archives of Computational Methods in Engineering **6** (1999) 71–116.

[15] A. H. Shah, K. C. Wong, S. K. Datta: Single and multiple scattering of elastic waves in two dimensions. J. Acoust. Soc. Am. **74** (1983) 1033–1043.

[16] S. K. Datta, A. H. Shah: Scattering of SH-waves by embedded cavities. Wave Motion **4** (1982) 256–283.

[17] J. B. Keller, D. Givoli: Exact non-reflecting boundary conditions. J. Comput. Phys. **82** (1989) 172–192.

[18] D. Givoli, J. B. Keller: A finite element method for large domains. Comput. Meth. Appl. Mech. Engng. **76** (1989) 41–66.

[19] D. Givoli, J. B. Keller: Non-reflecting boundary for elastic waves. Wave Motion **12** (1990) 261–279.

[20] V. R. Thiruvenkatachar, K. Viswanathan: Dynamic response of an elastic half-space to time-dependent surface tractions over an embedded spherical cavity. Proc. R. Soc. Lond. A **287** (1965) 549–567.

[21] H. Allik, T. J. R. Hughes: Finite element method for piezoelectric vibration. Int. J. Numer. Methods Eng. **2** (1970) 151–157.

[22] P. M. Morse, H. Feshbach: Method of theoretical physics. McGraw-Hill, New York, 1953.

[23] M. Abramowitz, I. A. Stegun: Handbook of mathematical functions. Dover publications, New York, 1972.

[24] O. C. Zienkiewicz: The finite element method, fifth edition. McGraw-Hill, New York, 1979.

[25] K. Washizu: Variational methods in elasticity and plasticity, second edition. Pergamon Press, Oxford, 1975.

[26] ATILA version 5.2.2, finite element code for piezoelectric and magnetostrictive tranducer and actuator modelling. User's manual. ISEN, Acoustics Laboratory, 2002.

[27] J. E. White: Underground sound. Elsevier Science Publ. Co., 1983. 193-210.

[28] M. Berraki, A. Baroni, B. Dubus: Numerical modelling of a buried directional seismic source. Proc. of SEG Meeting, 2004, 1889–1892.